PHYSICAL REVIEW ACCELERATORS AND BEAMS **22,** 070401 (2019)

Electrode contaminant plasma effects in 10^7-A *Z* pinch accelerators

D. R. Welch,[1] N. Bennett,[2] T. C. Genoni,[1] D. V. Rose,[1] C. Thoma,[1] C. Miller,[1] and W. A. Stygar[2]
[1]*Voss Scientific, LLC, Albuquerque, New Mexico 87108, USA*
[2]*Sandia National Laboratories, Albuquerque, New Mexico 87185, USA*

(Received 11 January 2019; published 8 July 2019)

The dynamics of electrode heating, sheath flow, and contaminant plasma evolution in Sandia National Laboratories' high-power *Z* accelerator is studied in a series of 2D relativistic particle-in-cell simulations. These dynamics can lead to the shunting of current before reaching the *Z* pinch load, thus degrading load performance. Previous work has focused on current diverted in the upstream magnetically insulated transmission lines (MITLs) and post-hole convolute regions of *Z*. In these regions, losses were found to scale strongly with load impedance as well as the system vacuum and were calculated to be as high as 1–2 MA. Downstream from the convolute region in *Z*, current measurement is problematic, leading to a lack of understanding of the loss mechanisms in the small radius (<3 cm) MITL feeding the load. In this paper, we present the first ever 2D fully electromagnetic, fully kinetic simulations of plasma evolution and current shunting in the inner MITL region of *Z*. This region is defined by a radially converging MITL, which is a feature common to MA-scale *Z* pinch accelerators. The electrodes in this region are rapidly heated via mainly Ohmic or skin depth heating. Plasmas quickly form, and surface contaminants are liberated as the temperatures exceed 700 K. Instabilities lead to a rapid plasma density fill of the inner MITL and subsequent current loss. The instability growth is likely due to the resistivity of the magnetized electrode plasma. The plasma, after exceeding 10^{15} cm^{-3} density, leads to an additional 1–2 MA current loss in the inner MITL region.

DOI: 10.1103/PhysRevAccelBeams.22.070401

I. INTRODUCTION

The *Z* accelerator at Sandia National Laboratories has successfully transported >25 MA current to a variety of loads. The electromagnetic power from four magnetically insulated transmission lines (MITLs) is combined in a double-post-hole convolute design into a single high-power MITL that drives the load [1–4]. As the power density increases, this "inner MITL" region is particularly susceptible to the degrading effects of Ohmic and charged particle heating and subsequent plasma ablation which can limit current delivery to the load. In this paper, we present first-of-a-kind calculations, using the particle-in-cell (PIC) simulation code Chicago, which provide insight in the physical mechanisms for plasma transport and current loss in the final inner MITL of the *Z* accelerator. Understanding these processes is crucial to the design of next-generation, higher current accelerators.

In a previous work [5,6], the scaling of current loss was explored under the assumption of quasiequilibrium operation using 3D PIC simulations of the radial MITLs and post-hole convolute region. In these regions, losses were found to scale strongly with load impedance as well as the system vacuum and were calculated to be as high as 1–2 MA. The upstream MITLs, post-hole convolute, and final vacuum transmission line were modeled as a coupled system. An electron sheath current launched from the cathode surfaces in the transmission lines upstream of the convolute flows along the Poynting vector (i.e., $\boldsymbol{E} \times \boldsymbol{B}$) streamlines into the convolute. It was also found that the magnitude of the sheath current flowing into the convolute largely determined the current loss in that system.

Downstream from the convolute post is a radially converging MITL supplying the full current to the load, which is a feature common to MA-scale *Z* pinch accelerators. Current measurement in this region is problematic [7], leading to a lack of understanding of the loss mechanisms at a small radius (<3 cm). Here, we present the first ever 2D fully electromagnetic, fully kinetic simulations of plasma evolution and current loss in the inner MITL region. The electrodes in the inner MITL region are rapidly heated via mainly Ohmic or skin depth heating. Plasmas quickly form, and surface contaminants are liberated as the temperatures exceed 700 K. The explosive electron emission and Ohmic heating of the surface cause desorption and ionization of adsorbed molecules on the cathode surface [8]. In the inner MITL, this process results

---

in fairly uniform high-density plasmas covering the entire cathode surface. Electrons pulled from this cathode plasma then generate the space-charge-limited (SCL) current. A plasma also arises on the anode surface from electron bombardment and Ohmic heating. In most PIC simulations, the thickness and motion of the electrode plasmas are neglected, and charged particles are assumed to be emitted directly from the surface with the SCL current. However, electrode plasmas can be created with thicknesses on the order of 100 μm with densities as high as 10^{17} cm^{-3} and can expand into the vacuum gap between the electrodes at velocities on the order of 1–3 cm/μs [8,9]. For 100-ns pulse lengths, plasma expansion can significantly impact inner MITL performance. Furthermore, microinstabilities lead to a more rapid plasma density fill of the inner MITL and subsequent 1–2 MA current loss.

In this paper, important MITL electrode physics is presented in Sec. II. In Sec. III, the new kinetic simulation technique designed to more accurately model electrode plasmas, implemented in the CHICAGO PIC code [10], is described. Results from CHICAGO kinetic simulations of the inner MITL of the *Z* accelerator are presented in Sec. IV and discussions in Sec. V.

II. INNER MITL ELECTRODE PHYSICS

For typical loads and drive voltages, the inner MITL region of the high-power *Z* accelerator experiences enormous energy densities on the electrode surfaces. From Ohmic heating alone, assuming a linear rise in the current density [11] and constant specific heat C_v, the electrode surface temperatures rise as $\Delta T = 8.0 \times 10^{-9} j^2/C_v = 203\, I^2/(r^2 C_v)$ for I in MA and r in centimeters. For $I = 10$ MA at $r = 2$ cm and $C_v = 3.756$ J/cm^3-K (stainless steel), we obtain $\Delta T = 1250$ K, which is near the melt temperature. Thus, contaminant plasmas, as well as metal vapor, boil off the electrodes well before the peak current (>20 MA on *Z*). The MITL-convolute system and blowup of the inner MITL, including key physical processes affecting the inner MITL performance, are shown schematically in Fig. 1. In addition to Ohmic heating, the electrode surfaces are heated by charged particle bombardment and radiation originating from the *Z* pinch load. While the radius at which melt occurs may vary, this type of electrode plasma desorption is common to MA-scale *Z* pinch accelerators.

As the temperature rises on a given surface, the adsorbed contaminants are desorbed with a rate determined by their binding energies. For example, typically water with a binding energy of 0.7–1 eV comes off first, followed by hydrocarbons and eventually CO, which has a higher binding energy. At the time of melt, in addition to the inventory of contaminant material, the electrode metal itself begins to vaporize or ablate and leaves the surface. Thus, there is a continuous flux of material entering the gap. The metal substrate material will follow the lighter and faster contaminant plasmas into the gap. Although contaminant plasma initially fills the gap and transports current loss, we expect that this substrate material motion will contribute to gap closure but not be the dominant effect at least until the surfaces are largely cleaned of the contaminant material. Thus, the metal ablation is not included in this paper but is a subject of future research.

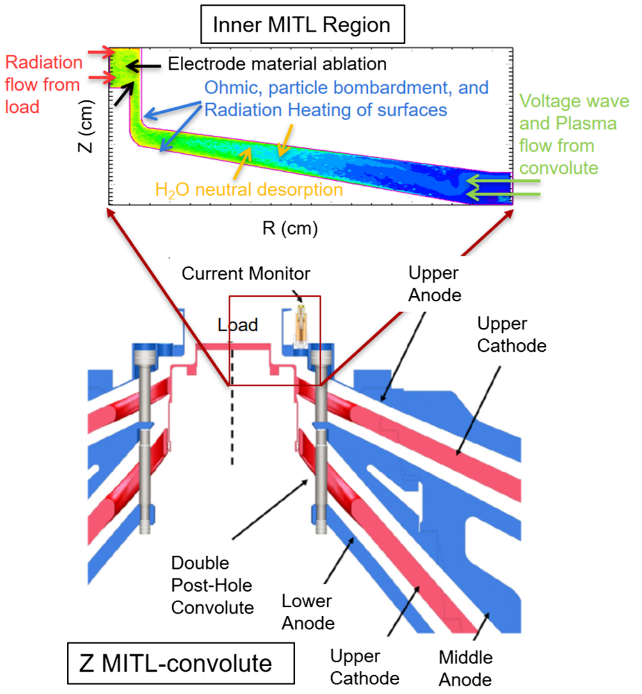

FIG. 1. A cylindrical (r, z) representation of the MITL-convolute system is shown. Power is delivered from four MITLs through a double-post-hole convolute to the load. An enlargement (top) of the radially converging inner MITL region is used to illustrate the physical processes which occur as power is delivered to a *Z* pinch. The voltage pulse and plasma generated upstream enter the inner MITL as shown on the right. The physical processes mapped by region are upstream charged particle flow, contaminant desorption, and ablation of material from the electrodes heated by Ohmic dissipation, charged particles, and radiation.

The typical bulk velocity of desorbed plasmas into the anode-cathode (AK) gap is of the order of 1-3 cm/μs [8]; however, lower-density plasma can move across the strong field lines much faster, even in the presence of strong magnetic fields. As described in Ref. [12], the physical mechanism driving the instability is a type of flute instability due to the opposite directions for electron and ion $v \times B$ force in a hard-edged resistive electrode plasma. The instability growth in idealized models of MITLs has been investigated by many authors. Swegle and Ott [13] considered the relativistic Brillouin (RB) flow equilibrium in the absence of a cathode plasma and found it to be susceptible to the magnetron instability which is localized at the position of a Doppler-shifted cyclotron resonance in the MITL electron sheath. Rose *et al.* [14] demonstrated that the strength of this instability is greatly reduced when MITL equilibria, determined self-consistently from PIC simulations, are used instead of the hard edged relativistic Brillouin model. Chang [15] extended the treatment to include a static cathode plasma. The resistive plasma was assumed to be thin, hard edged, and composed of infinitely massive ions. A low-frequency resistive instability ($\omega \ll \omega_{ce}$) due to the coupling of a negative energy slow wave in the MITL electron sheath with the resistive plasma layer was found in Chang's analysis. Chang's analysis of the resistive instability is performed for electromagnetic TM modes in which the wave propagates perpendicular to the equilibrium magnetic field when both the ion and electron Larmor radii are comparable to the scale length of the density gradient at the plasma edge, l_p. Simulations in Ref. [12] showed instability when including a finite ion mass which allowed for the diffusive expansion of the cathode plasma and formation of a plasma density gradient. In this paper, these simulations were done with an implicit algorithm verified against 1D cathode expansion models. The presence of a finite l_p also allows for the formation of ion drift instabilities [16], which can become significant when $\vec{B} \perp \nabla n$ and the ion Larmor radius are comparable to l_p. The ion drift instability results in flutelike density perturbations which permit transport across $\vec{B}$.

III. COMPUTATIONAL TECHNIQUES USED IN INNER MITL SIMULATIONS

A. Electrode desorption model in CHICAGO

In a transmission line, there are initially no free current carriers, and the incoming electromagnetic wave results in an increasing applied AK voltage and electric field stress. The surface heats continuously from Ohmic heating as described in Ref. [11], where the thermal conductivity and specific heat are assumed to be constant. For typical bare metal surfaces, electrons are emitted from the cathode above an electric field threshold of roughly 250 kV/cm. As the threshold is exceeded, the surface breaks down explosively, yielding a surface plasma. In the unified electrode model used in CHICAGO, the explosive breakdown of the cathode increases the surface temperature by 100° (an adjustable parameter in the model). This temperature rise is a relatively small contribution compared to the 400 °C temperature rise required for plasma formation but is meant to speed plasma formation. The cathode plasma is then desorbed thermally and can then provide a source of electrons for acceleration across the AK gap. The plasma is assumed to be comprised of water molecules which are a significant constituent of surface contaminants. A completely fragmented and ionized water plasma ($3e^-$, $2H^+$, O^+) is produced within a cell of the material surface. The model is based largely on the experimental results of Li and Dylla [17] and Dylla, Manos, and LaMarche [18] and the theoretical analysis of La Fontaine [19].

After cathode electrons are accelerated across the AK gap, electron impact contributes to the Ohmic heating of the anode surface. Typically, when the anode surface temperature rises by 400 °C, neutral atoms are liberated from the surface. As with the cathode, these desorbed particles are assumed to be from water adsorption. The desorption of H_2O from the surfaces of the diode can be concisely treated using the Temkin isotherm [19,20], which depends only the gas pressure p. From the pressure, the initial number of monolayers is calculated to be

$$N_{\mathrm{ML}} = \max[8.04p^{0.099} - 1.536, 0], \tag{1}$$

where p is in Torr and 1 monolayer is defined as 8×10^{15} molecules/cm^2 (note that 10^{15} cm^{-2} is typically used for ideal smooth surfaces, but machined stainless-steel surfaces may have 8 times the number of binding sites) [21]. The binding energy increases for deeper adsorbed material. The effective binding energy E' is given by

$$E' = 1 - \chi N_{\mathrm{ML}}, \tag{2}$$

in eV. In an analysis of the Li and Dylla [17] data, Redhead [22] found the value $\chi = 0.5$. In our simulations, we find that a choice of $\chi = 0.17$ better reproduces the experimentally observed time dependence of loss current in high-power post-hole convolute simulations [23]. Finally, the desorption rate is found from the standard Arrhenius thermal desorption formulism:

$$R = 10^{13} N_{\mathrm{ML}} e^{-11600E'/T_s}, \tag{3}$$

where T_s is the surface temperature. We assume the liberated neutrals rapidly ionize and dissociate (within a grid cell length) via impact ionization and avalanche in a staged ionization [24]. From Eq. (3), as the surface heats, the time of rapid desorption and plasma formation scales linearly with E'. The Temkin model has recently been compared with molecular dynamics simulations showing reasonable agreement [25]. The accuracy of the two assumptions, (i) material in the MITL gap is largely contaminants such as water and (ii) neutrals are rapidly ionized after desorption, are the subject of future work.

It should be noted that, although the desorption model breaks down as the surface approaches melt, the vast majority of adsorbed water is liberated by this time. As discussed in the previous section, vaporization of the electrode bulk metal is not included in this paper.

B. Magnetic implicit PIC algorithm

The simulations presented here used a new technique that combines the implicit time integration of the direct implicit (DI) technique [26,27] for large plasma frequencies (ω_p) with the highly accurate orbit integration properties

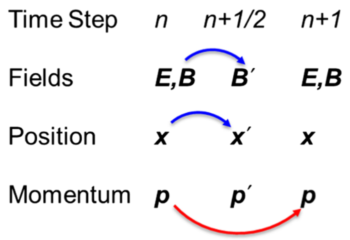

FIG. 2. The time centering for the MI algorithm is shown schematically for both fields and particles. The first pushes of fields and particles are shown via blue arrows to interim (x', p') or half step (B') positions.

at a large cyclotron frequency (ω_c) of the magnetic implicit (MI) algorithm [28].

Charged particle orbits in magnetic fields can be complex and chaotic. Standard explicit PIC techniques making use of the Boris push [29] do not properly describe particle orbits when the product of the cyclotron frequency and time step $\omega_c \Delta t$ is significant. While largely accurate in the calculation of $E \times B$ drift velocities, the Boris push overpredicts the cyclotron radius and underpredicts the gradient B drift and mirror force with errors scaling roughly as the square of $\omega_c \Delta t$. Here, we describe an efficient algorithm that can greatly relax this constraint and is applicable to massively parallel simulation codes. The MI algorithm differs from standard PIC in that the motion of a charged particle in an electromagnetic field is calculated with the position and relativistic momentum of the particle calculated at the same time level. The MI method preserves the correct particle cyclotron radius for large time steps ($\omega_c \Delta t \gg 1$). MI does not require explicit calculation of the particle magnetic moment or additional field calculations to determine the local transverse and longitudinal magnetic field gradients. In addition, the usual magnetic field rotation matrix is modified to conserve energy and corrects for the mirror force in regions where a significant longitudinal magnetic field gradient exists. After the particle momentum is advanced, an effective velocity which includes a correction for particle drift in a transverse magnetic field gradient is calculated and used to advance the particle position.

Both fields and particles are pushed twice per time step. The time centering is shown in Fig. 2. Because our push now is centered about the full time steps, in order to construct the rotation tensor for each particle at the centered $n + 1/2$ step, a full time step advance of B constructed at the $n - 1/2$ step is done with an explicit advance of Faraday's equation with E^n:

$$\frac{B^{n+1/2} - \frac{1}{2}(B^{n-1} + B^n)}{\Delta t} = -\nabla \times E^n, \tag{4}$$

solving for $B^{n+1/2}$.

In the first particle push, the particle position and momentum are advanced by

$$p' = p^n + \frac{q\Delta t}{2m}\left[E^n + \frac{(p^n + p')}{\gamma^{n+1/2}c} \times B^{n+1/2}\right] \quad \text{and}$$
$$x' = x^n + \frac{\Delta t}{2}\left[\frac{(p^n + p')}{\gamma^{n+1/2}c}\right], \tag{5}$$

where the particle charge, mass, and relativistic factor are q, m, and γ, respectively. In this step, the momentum and position are advanced to p' and x' assuming $E^{n+1} = 0$. Thus, the current density calculated in this step, $J^{n+1/2}$, is the result of all known field quantities. Note that the use of B at the $n + 1/2$ step necessitates both the $1/2$ step Faraday and position advance. In the first push, this field is properly centered in time and space. We find this half advance to have a small effect, since, if B is not advanced, it is later corrected in the second push. For the calculation of the implicit terms, the MI first particle push resembles the DI algorithm in that it calculates a local susceptibility tensor $\langle S \rangle$ which is necessary to solve both the electromagnetic and electrostatic fields with future field corrections for currents and charge densities, respectively. In contrast to the MI integration, the temporal stencil of the DI time integration replaces E^n with E^{n-1} and $B^{n+1/2}$ with B^n in Eq. (5). In both cases, the future electric field is taken as $\boldsymbol{E}^{n+1} = 0$ in the first particle push. At the intermediate position x', the linearized response of the particle to this field is accounted for in the field advance by summing the susceptibility of each particle at each cell edge for the three directions, giving [30]

$$\langle \boldsymbol{S} \rangle = \frac{\rho \Delta t q}{2\gamma_{n+1/2} m} \langle \boldsymbol{T} \rangle (I - \mathbf{v}_{n+1/2}\mathbf{v}_{n+1/2}), \tag{6}$$

where the rotation tensor $\langle T \rangle$ is given by

$$\langle T \rangle = \frac{1}{1 + \Omega^2}\begin{bmatrix} 1 + \Omega_1^2 & \Omega_1\Omega_2 + \Omega_3 & \Omega_1\Omega_3 - \Omega_2 \\ \Omega_1\Omega_2 - \Omega_3 & 1 + \Omega_2^2 & \Omega_2\Omega_3 + \Omega_1 \\ \Omega_1\Omega_3 + \Omega_2 & \Omega_2\Omega_3 - \Omega_1 & 1 + \Omega_3^2 \end{bmatrix}, \tag{7}$$

and $\Omega = \Delta t q \boldsymbol{B}^{n+1/2}/(2\gamma m c)$.

After the first particle push, Ampere's equation is modified to account for the current density due to the future electric field:

$$\frac{E^{n+1} - E^n}{\Delta t} = \frac{1}{\varepsilon}\left(\nabla \times \frac{B^n + B^{n+1}}{2\mu}\right) - \boldsymbol{J}^{n+1/2} - \langle \boldsymbol{S} \rangle \cdot E^{n+1}, \tag{8}$$

by including the last term $\langle \boldsymbol{S} \rangle \cdot E^{n+1}$ for the current due to the future field only. Along with Faraday's equation,

$$\frac{B^{n+1} - B^n}{\Delta t} = -\frac{1}{2}\nabla \times (E^n + E^{n+1}), \tag{9}$$

the new fields are solved via an iterative matrix inversion technique such as general minimum residual (GMRES).

C. Poisson correction

Because the current density summed in the second particle push can deviate from the $\langle S\rangle \cdot E$ term, an error can build up in the charge conservation. Previously, we had kept track of this error and slowly added it into $\boldsymbol{J}$ in subsequent steps [27]. This introduced a phase lag in the current from the actual particle motion and limited the accuracy of the algorithm. We have long speculated that this lag is responsible for the observed particle energy cooling and time step constraints, i.e., $\omega_c \Delta t < 0.4$ when $\omega_p \Delta t \gg 1$. Discussed in Ref. [31], we have avoided the method of Poisson correction due to the lack of adequate linear solvers until now. The implicit electrostatic equation is derived by applying the $\nabla \cdot$ operator to Eq. (8). We can more rigorously correct for the charge density error within a time step (ρ_{err}) and remove this lag via a Poisson correction calculation immediately after the electromagnetic solution:

$$\nabla \cdot (1 + \langle S\rangle) \cdot \nabla \Psi_{\mathrm{err}} = \rho^0_{n+1} - \nabla \cdot (1 + \langle S\rangle) \cdot E'_{n+1} = \rho_{\mathrm{err}}, \tag{10}$$

which gives a corrected field for the final particle push

$$E_{n+1} = E'_{n+1} - \Delta \Psi_{\mathrm{err}}, \tag{11}$$

where the electric field after the EM push is E'_{n+1} and ψ_{err} is the "error" potential associated with ρ_{err}. The $\langle S\rangle$ tensor couples all the electric field directions through the local B field, yielding an elliptical equation of 19 terms in 3D.

D. Final particle push

Finally, in the final or correction push, the particles are advanced once again from their initial conditions at step n using the old fields and newly calculated $\boldsymbol{E}^{n+1}$ and $\boldsymbol{B}^{n+1}$. This second advance is now identical to that discussed Ref. [28] and will not be repeated in detail here. The mirror force and gradient B corrections are done in the frame of the magnetic field direction of each particle. MI requires no explicit calculation of the particle magnetic moment or additional field calculations to determine the local transverse and longitudinal magnetic field gradients. The usual magnetic field rotation matrix is modified to conserve energy and corrects for the mirror force in regions where a significant longitudinal magnetic field gradient exists. After the particle momentum is advanced with all full time step fields,

$$p^{n+1} = p^n + \frac{q\Delta t}{2m}\left[(E^n + E^{n+1}) + \frac{(p^n + p^{n+1})}{2\gamma^{n+1/2}c} \times (B^n + B^{n+1})\right], \tag{12}$$

an effective velocity $\beta'_{\mathrm{eff}}c$ which includes a correction for particle drift in a transverse magnetic field gradient, $\beta'_d c$, and is used to advance the particle position,

$$x^{n+1} = x^n + \beta'_{\mathrm{eff}} c \Delta t, \tag{13}$$

where

$$\beta'_{\mathrm{eff}} = \beta'_d + \frac{p^n + p^{n+1}}{(\gamma^n + \gamma^{n+1})c}. \tag{14}$$

Deviations in this final step from the predicted currents (and charges) due to the future electric field in Ampere's equation of Eq. (8) [and Poisson equation of Eq. (10)], including these second-order drift corrections due to mirror force and gradient B drift, are corrected in the Poisson correction of the subsequent time step.

IV. KINETIC INNER MITL SIMULATIONS

The algorithms discussed in Sec. III are applied to simulations ranging from simple benchmarking problems to inner MITL designs fielded on Z. We use the new magnetic implicit algorithm as well as the older DI and explicit algorithms for comparison. Plasma is created in three ways: direct injection through a boundary, space-charge-limited emission from surfaces, and thermal desorption from a surface using the Temkin model for injection of neutral H_2O flux into the vacuum, where we assume for stainless steel 1 monolayer is effectively 8×10^{15} water molecules per cm^2.

A. Cathode plasma evolution test for new MI algorithm

We first compare the evolution of a cathode plasma in a simple coaxial transmission line. The cathode and anode surfaces are at 2- and 2.25-cm radii, respectively. Cathode surface dynamics including SCL emission and thermal desorption (gas pressure of 10^{-6} Torr) are enabled over a 4-cm axial extent. Although the transmission line has a 7-Ω vacuum impedance, the input and output boundary impedances are 0.7 Ω. This difference creates turbulent behavior, as in an actual Z power feed. The simulations are run with the benchmarked DI algorithm [12], the new MI algorithm detail in Sec. III, and a standard energy-conserving explicit algorithm. Each simulation has 50-μm spatial resolution, which is adequate to model the electrode plasma dynamics in these and subsequent larger-scale simulations. The explicit simulation is run with a time step $\Delta t = 3.33 \times 10^{-5}$ ns,

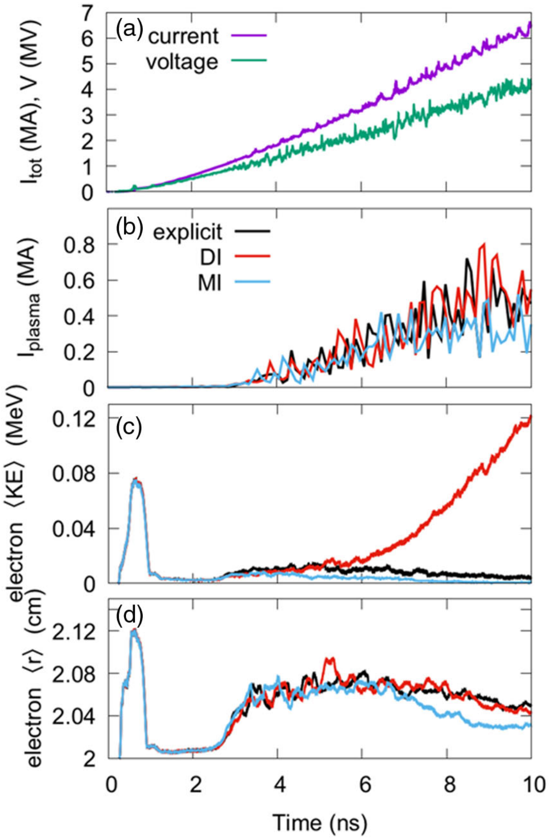

FIG. 3. Comparison of three particle push algorithms (DI, MI, and a standard energy-conserving explicit algorithm) applied to cathode plasma generation in a 7-Ω coaxial transmission line. Plotted are (a) the load current and voltage, (b) the plasma current, (c) the mean electron energy, and (d) the mean electron radial extent averaged over 1 cm axially.

which is 5 times smaller than the time step used in the implicit algorithms and permits the resolution of cyclotron ($\omega_c \Delta t < 0.4$) and plasma ($\omega_p \Delta t < 0.5$) frequencies.

The coaxial transmission line is driven for 10 ns with a linearly rising pulse peaking at 4.5 MV and 6 MA, as plotted in Fig. 3(a). The plasma dynamics are similar for each algorithm tested. As shown in Figs. 3(b) and 3(d), there is 1 ns between the initiation of electron emission and magnetic insulation, the plasma current rises to 500 kA, and, after insulation, the plasma radial extent (mean transverse extent from the cathode) has a 0.07 cm maximum before falling as the magnetic pressure increases. The largest variation between the three algorithms occurs in the mean electron energy [Fig. 3(c)]. At 5 ns where $\omega_c \Delta t = 1$, the electron energy in the DI algorithm rises where the energy in the other two falls due to their location in the AK gap potential. We attribute the difference in Fig. 3(c) between the explicit and MI simulations to increased statistical particle noise in the explicit simulation. Noise in the implicit simulations is reduced by $1 + 1/2(\omega_p \Delta t)^2$ due to the susceptibility term in the field equations. We tested convergence with the MI algorithm by reducing the time step and spatial cell sizes to 25 μm. The finer resolution simulation results for electron energy and height were within 10% of the 50-μm simulation, and the plasma current was within 20%.

Details of the spatial distribution of electrons and protons from the MI algorithm are illustrated in Fig. 4. The plasma initially evolves to a 150-μm thickness along the cathode. After the initial quiescent stage at 1 ns, the plasma rapidly becomes unstable and nearly fills the gap. By 3 ns, the plasma begins interacting with the sheath in a highly nonlinear fashion. The plasma is likely unstable to both the resistive instability discussed in Sec. II but also the flutelike or magnetron instability. These instabilities feed large electron vortices which initially attract ions from the plasma. The ions, when subsequently exposed after the vortex leaves, partially return to the cathode but with significantly more energy and heat the plasma. The plasma ions have nearly reached the anode by 10 ns with a density of roughly 10^{15} cm^{-3}. We believe this combination of plasma and sheath instabilities is found throughout the inner MITL region, although smaller gaps will lead to more rapid evolution and filling of the gap.

To better understand the instability mechanism, we now apply a uniform B_z field ranging from 3 to 10 T in the 2D MITL MI simulations. The applied field is the order of that of the peak $B_\theta = 6.5$ T driven magnetic field at 10 ns. As discussed in Sec. V, this applied field turns the parallel magnetic field towards the direction of the plasma current. Shown in Fig. 5, as the applied magnetic field approaches that of the driven field, the cathode plasma and electron sheath become more laminar. We also looked at a 3D simulation of the MITL at the 10 T applied field and saw a nearly identical suppression of the field. These observations have implications on the nature of the plasma-sheath instability.

B. Simulations of *Z* Inner MITL

In the CHICAGO simulations of the *Z* scale inner MITL, we use the Poisson-corrected MI algorithm. A model of the *Z* power pulse is provided by a circuit external to the simulation grid, as described in Ref. [5]. This circuit models idealized behavior for the outer MITLs and post-hole convolute region. The surface physics includes Ohmic and particle heating with water desorption. For completeness, we include a representative neutral plasma flow of electrons and protons from the transmission lines upstream calculated in detailed 3D simulations [5] to be roughly 0.5 MA with a linear 110-ns rise and skewed towards the anode (the mean plasma position is 70% across the gap). This injection of plasma is intended to provide a mature plasma flow at a large radius which would otherwise require some distance to evolve. The main effect is to increase the temperature rise at the electrodes due to charged particle impact heating. In the 2D simulations, a 20 mΩ load is applied at the large axial position along the inner radius.

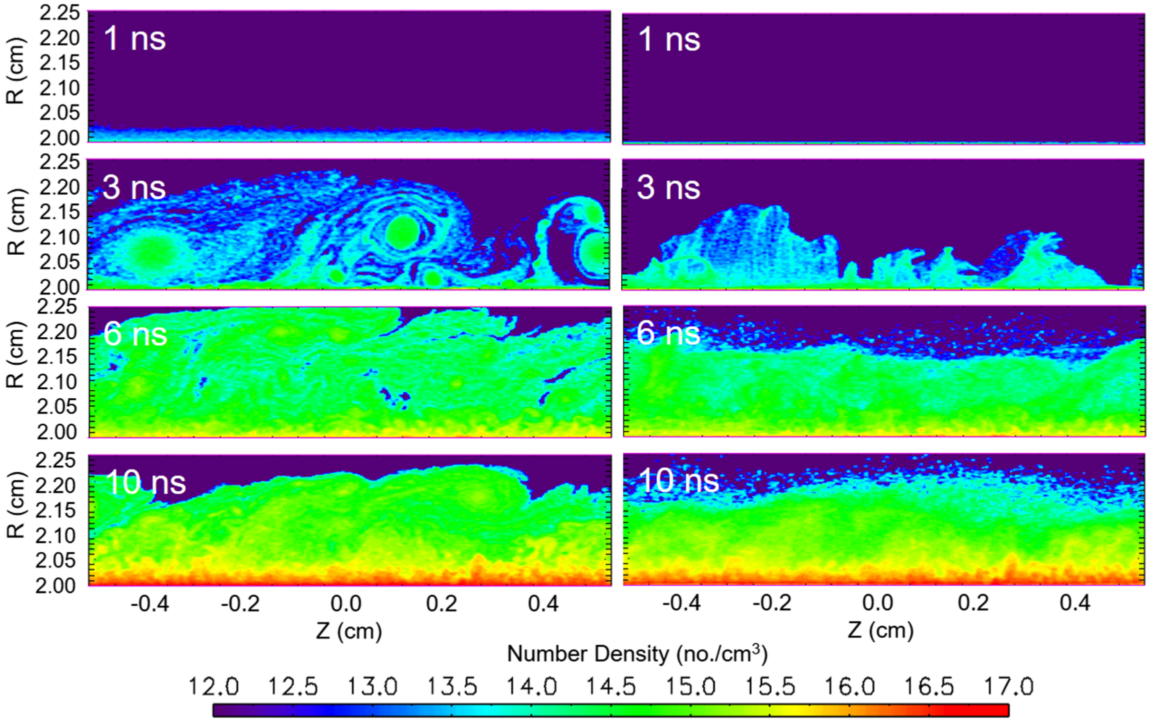

FIG. 4. In the MI transmission line simulation, the evolution of the electron density (left) and proton density (right) from 1 to 10 ns is plotted. The plasma evolves from the cathode (bottom electrode).

C. Power flow 18a inner MITL simulation

A series of shots fielded on Z to test power flow issues are referred to as the power flow 18a series. The inner MITL region for this series offers a significant surface area from which to inject desorbed water. Using the local current density and Knoepfel analytic formula [11] for Ohmic heating of stainless steel, we see in Fig. 6 that, out to $r = 10$ cm, we expect desorption and plasma formation (400° surface temperature rise) [32] with surface melt occurring for $r < 5$ cm. Charged particle heating will reduce the time to these temperatures somewhat. However, most

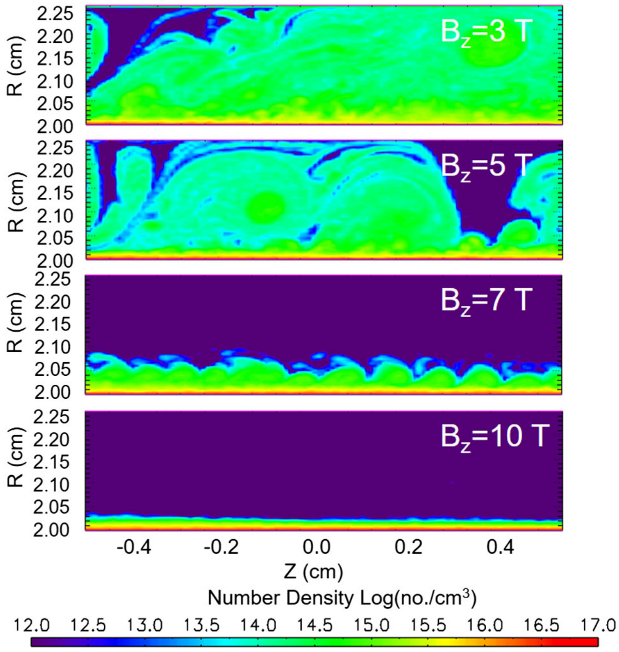

FIG. 5. A B_z field is applied ranging from 3 to 10 T and the electron densities plotted after 10 ns. The injected current produces a peak $B_\theta = 6.5$ T.

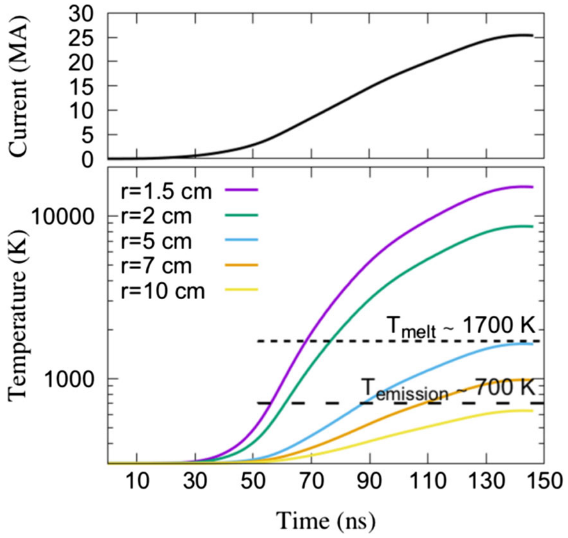

FIG. 6. Using the Knoepfel Ohmic heating equation [11] for applied current, the temperature at various radii is plotted for a typical Z pulse. Note the 700° point for typical plasma formation and the melt temperature for stainless steel.

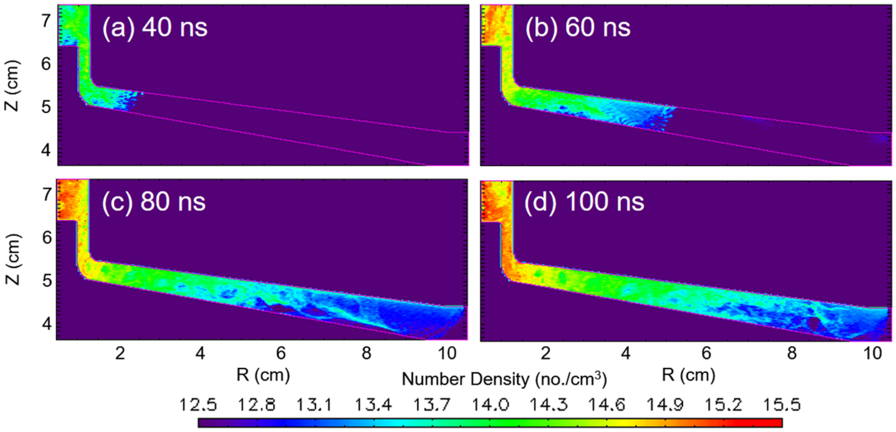

FIG. 7. For the $p = 0$ Torr simulation, the ion density is plotted at (a) 40, (b) 60, (c) 80, and (d) 100 ns. Electron space charge limited emission allows for field stress $\mathrm{E} = 200\,\mathrm{kV/cm}$. Ions H^+ and O^+ SCL emission allowed after surface heats to 700 K.

of the surface inventory of contaminants will be desorbed into the vacuum region over the Z pulse time.

Using the Temkin desorption model, we assumed gas pressures of $p = 0$ and 10^{-5} Torr. With $p = 0$, there is only SCL emission of electrons after $E = 200\ \mathrm{kV/cm}$ and H^+ and O^+ after the anode has heated to 700 K. For $p = 10^{-5}$ Torr, there is a monolayer of water on all surfaces which may desorb and form a dense electrode plasma. The simulations were run to near peak power at 100 ns. The ion density for $p = 0$ (Fig. 7) reaches a peak density of $3 \times 10^{15}\ \mathrm{cm}^{-3}$ near the axis. At smaller radii, the ions are emitted sooner and augmented by ions swept downstream by the ponderomotive force. For $p = 10^{-5}$ Torr, more ions are available to accumulate. The density, shown in Fig. 8, reaches a peak of $10^{17}\ \mathrm{cm}^{-3}$ by 100 ns and is still growing, while for $p = 0$ Torr the density has plateaued. In addition to a higher ion density in the gap, $p = 10^{-5}$ Torr also generates a high-density surface plasma expanding into the gap.

The calculated differences in plasma evolution between pure SCL emission (Fig. 7) and Temkin desorption (Fig. 8) change the current delivered to load. Figure 9(a) shows the current delivered to the load reaches 18.1 MA for $p = 0$ and 17.4 MA delivered at $p = 10^{-5}$ Torr. The difference between the injected and load currents for both simulations is plotted in Fig. 9(b). The calculated loss current in the two simulations deviates after 80 ns, reaching nearly 0.85 MA at 100 ns at the high pressure. The 2D map of net current in Fig. 9(c) shows the location of current loss for the $p = 10^{-5}$ Torr simulation. The losses are largely at $r < 3$ cm.

D. MagLIF 17b inner MITL simulation

A second series of shots fielded on Z that is interesting for inner MITL plasma evolution is the MagLIF (magnetized linear inertial fusion) 17b series. In the MagLIF experiments on Z, a solenoidal magnetic field is applied to reduce energy transport within the fuel for fusion yield [33]. The inner MITL in the 17b experimental series was

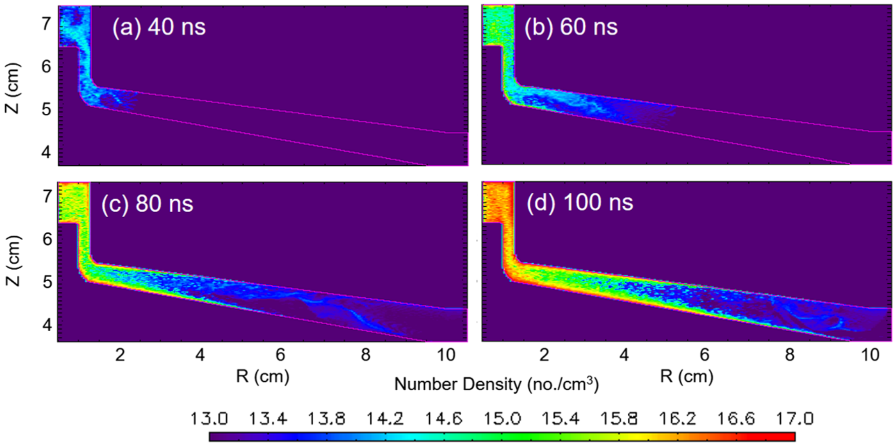

FIG. 8. For the $p = 10^{-5}$ Torr simulation, the ion density is plotted at (a) 40, (b) 60, (c) 80, and (d) 100 ns. Plasma desorbed via the Temkin model.

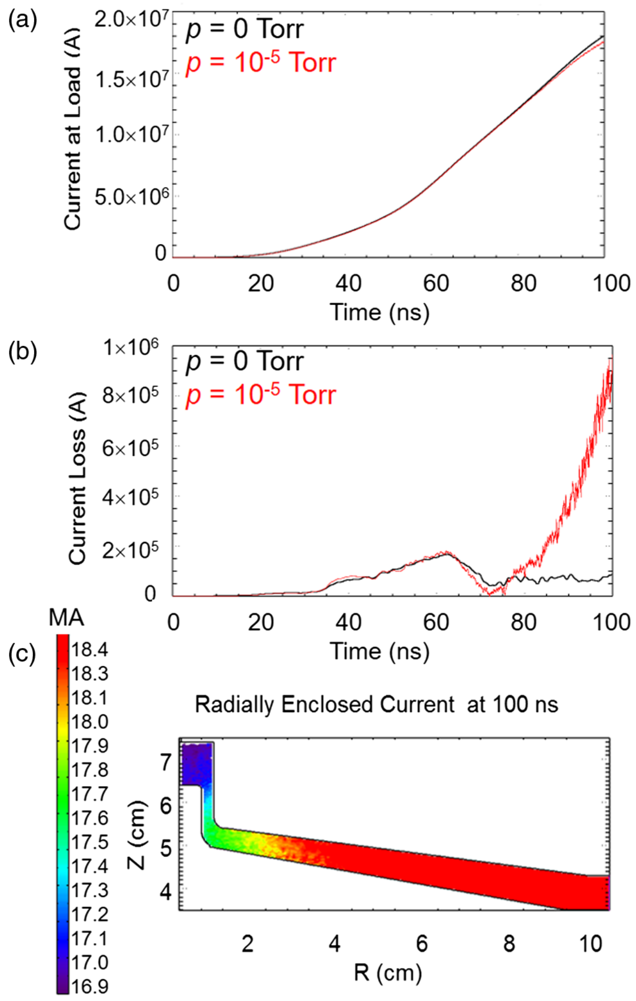

FIG. 9. For the two 18a inner MITL simulations, (a) the current delivered to the load ($z = 6$ cm), (b) the current loss before reaching the load, and (c) the current transported to a given position (radius-B_θ product) in the MITL after 100 ns is plotted for the $p = 10^{-5}$ Torr simulation.

designed to be a test of a lower inductance inner MITL design, meaning a smaller MITL length and gap width. A plot of the dynamic electric fields (peak 400 kV/cm) at 20 ns is shown in Fig. 10(a) along with a realistic field map of the applied solenoidal fields (peak 1.4 T field) in Fig. 10(b). The electric and applied magnetic fields are nearly orthogonal at $r = 3$ cm, which provides good insulation. This geometry with applied solenoidal fields was driven by the same basic circuit, taking into account the changes in inductance through the convolute. As with the 18a simulation, a small 20-mΩ impedance approximates the early-time load, and a 0.5-MA (110-ns linear rise time) peak plasma current is injected at the outer radial boundary modeling plasma flowing from the convolute. Simulations with and without the applied B at 10^{-5} Torr gas pressure are used to determine the effect of the applied B insulation. In addition, simulations without applied B were run at $p = 10^{-6}$ ($\mathrm{N_{ML}} = 0.5$) and 10^{-10} Torr ($\mathrm{N_{ML}} = 0$) to assess the benefits of reduced pressure on current losses.

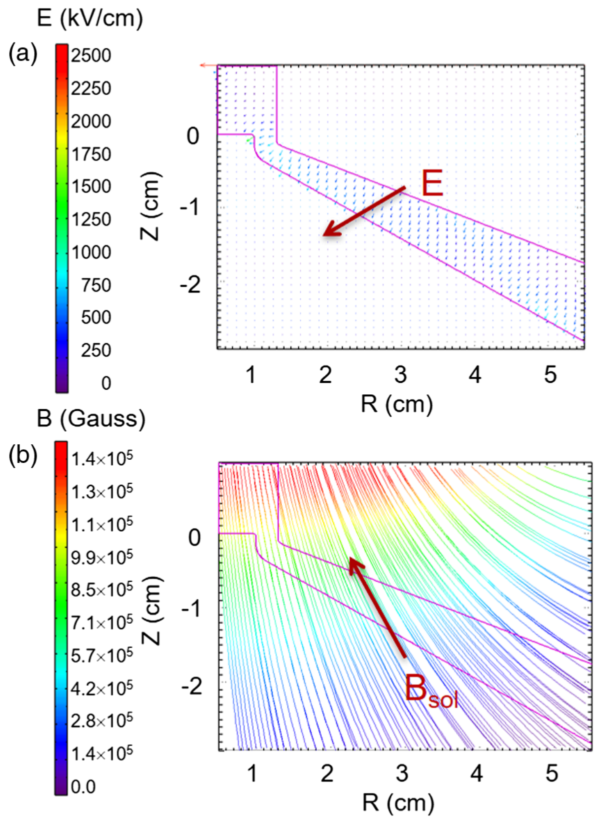

FIG. 10. The electric field vectors (a) and the applied magnetic field (b) at 25 ns in the Z pulse are plotted for the 17b inner MITL. The characteristic vectors across the gap are indicated by E and B_{sol} in the plots.

The results for peak current diverted from the load at 100 ns are summarized in Fig. 11. The magnetized simulation at 10^{-5} Torr ($N_{\mathrm{ML}} = 1$ or 8×10^{15} water molecules) performed better than all but the smallest pressure unmagnetized simulation. With magnetization, only 460 kA current

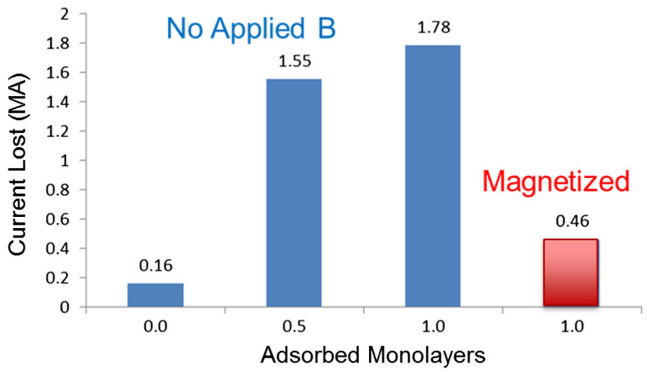

FIG. 11. The peak current loss (after 100 ns) in the 17b geometry is shown for unmagnetized and magnetized MITL and adsorbed surface water. Note that $N_{\mathrm{ML}} = 1$ has 8×10^{15} water molecules.

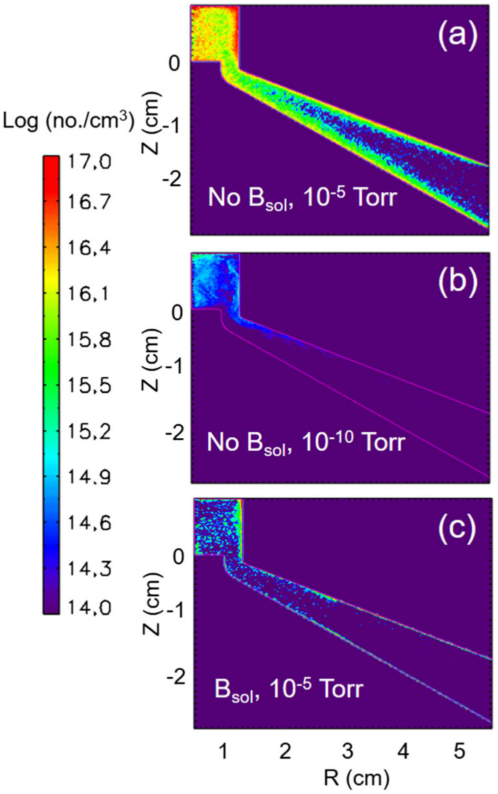

FIG. 12. For (a) 10^{-5} Torr ($N_{ML} = 1$) and (b) 10^{-10} Torr ($N_{ML} = 0$) gas pressure with no applied B and (c) 10^{-5} Torr gas pressure with applied B, the total ion density is plotted after 100 ns.

was lost, nearly a factor of 4 less than unmagnetized. Reducing the pressure an order of magnitude without magnetization reduced the loss only by 230 kA. Reducing the pressure down to 10^{-10} Torr (no adsorbed water) reduced the losses to 160 kA. Unfortunately, this gas pressure and adsorbate level is not feasible in experiments.

The benefit provided by an applied B field is seen in Fig. 12, where the electron density after 100 ns is plotted for no applied B at 10^{-10} Torr gas pressure, no applied B at 10^{-5} Torr, and an applied B at 10^{-5} Torr. The simulations without an applied B field have similar plasma dynamics to the previous 18a simulation. There is plasma diffusion throughout the inner MITL with densities reaching 10^{17} cm^{-3} near the surface at the load. Significant plasma fills the AK gap for radii <2 cm. It is in this region that the bulk of the nearly 2-MA current is lost. It is interesting to compare this loss with the ~1-MA current loss at roughly the same current and 3-mm minimum gap calculated in the 18a simulation at the same vacuum pressure. The key difference here is that the induced voltage is only 1/2 as large in the 18a simulation (1000 versus 2300 kV in the higher inductance MITL of 17b). The higher voltage clearly conducts more current, assuming similar plasma conditions. When the gas pressure is reduced to 10^{-10} Torr with zero surface adsorbates, the plasma density is 2 orders of magnitude smaller, resulting in the smaller current loss also observed in the 17b simulation. In this case, the amount of liberated plasma is basically that of the SCL current. Most of the loss is due to injected plasma at 5.5-cm

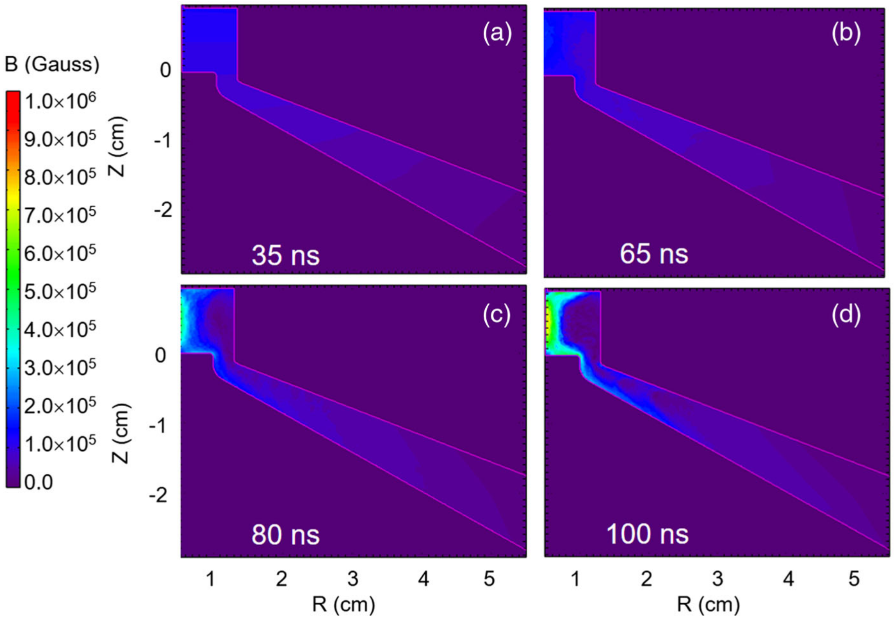

FIG. 13. The solenoidal field is plotted for the 10^{-5} Torr pressure with applied B field simulation at (a) 35, (b) 65, (c) 80, and (d) 100 ns.

radius reaching the electrodes. Increasing the gas pressure to 10^{-5} Torr but turning on the applied B field gave nearly as low a current loss. In this case, the plasma is mostly confined to the electrode surfaces and does not diffuse far into the gap, although this plasma is 10^{17} cm^{-3} at those surfaces. The applied solenoidal magnetic field increases the conductivity in the direction of the current. Thus, the enhanced stability is consistent with the resistive plasma instability [15].

Despite the stronger insulation of plasma in the applied B simulation, the magnetic field (A_θ) flux is strongly compressed up against the load similar to that seen in Ref. [34] with an extended magnetohydrodynamical model. The evolution of the solenoidal field is shown in Fig. 13. The flux is increased nearly 2 orders of magnitude reaching 100 T at 100 ns. The plasma (plasma is above 10^{15} cm^{-3} density and 1 keV temperature near the load) flow in the 10^{-5} Torr pressure simulation drives a diamagnetic current which strongly compresses the field. With only SCL electron and ion emission, the flux compresses only 10%. The modification of the applied flux strongly affects the heating due to Ohmic and plasma impact. This heating has been proposed as a mechanism for perturbing the thermal-electric and magnetic Rayleigh-Taylor instabilities. The measured density profiles on MagLIF experiments exhibit a helical structure [35]. To more accurately predict the perturbation requires a 3D simulation including the detailed plasma evolution.

V. DISCUSSION AND SUMMARY

In this paper, we have presented detailed simulations and analysis of plasma transport and current loss in the inner MITL of the Z accelerator using the new magnetic implicit kinetic algorithm. The processes included in the simulation model are charged particle flow, contaminant desorption from the electrodes heated by Ohmic dissipation, and particle impact. When an adsorbed contaminant inventory corresponding to a gas pressure 10^{-5} Torr is assumed, a plasma density reaching 10^{17} cm^{-3} is transported across the intense magnetic field of the 20 MA accelerators. This transport is largest when the conductivity in the direction of the current is low, i.e., perpendicular to the magnetic field:

$$\sigma_\perp = \sigma_\parallel \frac{1}{1+\frac{\omega_c{}^2}{\nu_m{}^2}}, \tag{15}$$

where $\sigma_\parallel = e^2 n_e / m_e \nu_m$ is the conductivity along the field line and ν_m is the momentum transfer frequency of the electrons. In the expected 100 T fields at 20 MA, $\sigma_\perp$ can be orders of magnitude smaller than $\sigma_\parallel$. This reduction is an important clue when inferring the presence of the magnetron or resistive plasma instabilities.

Chang *et al.* [15] carried out analytic calculations of the stability of TM wave in the combined cathode plasma–electron sheath system. They observed a coupling of the low-frequency electron sheath waves with a thin resistive plasma layer resulting in a broad spectrum of unstable low-frequency ($\omega < \omega_{ce}$) modes. Although calculated for higher impedance transmission lines, the theory suggests the strong possibility that such a mechanism is at play in our inner MITL simulations. Rose *et al.* [36] have generalized the Chang model to account for a more realistic electron sheath density profile. Using this technique and including the full conductivity tensor appropriate for a magnetized plasma [using $\sigma_\parallel$ and $\sigma_\perp$ from Eq. (15)] requires numerical integration across the plasma layer and electron sheath in a shooting method formulism to determine the eigenfrequencies. These preliminary calculations have been carried out for the 4.5 MV, 6 MA MITL coaxial plasma simulations discussed in Sec. IV. Assuming a representative thin plasma layer (200 μm with 3 eV temperature and 10^{16} cm^{-3} density) between the cathode and electron sheath, a broad spectrum of unstable modes is found. Growth rates are robust with e-folding times of <1 ns. These preliminary results are consistent with Chang (see Fig. 3 in Ref. [15]) and with the simulation results for the coaxial plasma simulation. The simulations show that the instability feedback with the plasma accelerates transport across the strong magnetic field. Assuming a constant impedance of 0.7 Ohm and varying the voltage, the instability times are shown in Fig. 14. With assumed density profiles for both the plasma and electron sheath shown, the growth time falls rapidly with voltage. This is consistent with the sudden onset of instability near 3 ns in the coaxial plasma simulation shown in Fig. 4. The application of a field in the direction of the current flow ($B_z = 3$–10 T) increases σ_z orders of magnitude with a significant portion of $\sigma_\parallel$ in that direction. The effect in the simulations shows increasing suppression of the instability as the field approached the driven 6.5 T field. The instability growth times and dependence on conductivity strongly support the presence of the resistive plasma instability.

The rapid growth of resistive plasma instability and subsequent plasma ion motion into the gap rapidly fills the MITL gap with a 10^{15} cm^{-3} density plasma. Given a sufficient surface area and the strong ponderomotive force on the plasma, the plasma is swept downstream, magnifying the density and leading to significant current loss (1–2 MA) just upstream of the load in the 18a and 17b inner MITL simulations.

The current diverted from the load is weakly sensitive to gas pressure when using the Temkin isotherm desorption model in CHICAGO. This behavior is expected given the tenth power dependence of adsorbed monolayers with pressure [see Eq. (1)]. The 2D simulations including the initial solenoidal field for the MagLIF loads (17b geometry) yield significantly less plasma accumulation downstream and current loss. This result is further evidence for the presence of the resistive plasma instability. Although the applied 10 T field is an order of magnitude smaller than the azimuthal magnetic field near the peak current, as in the

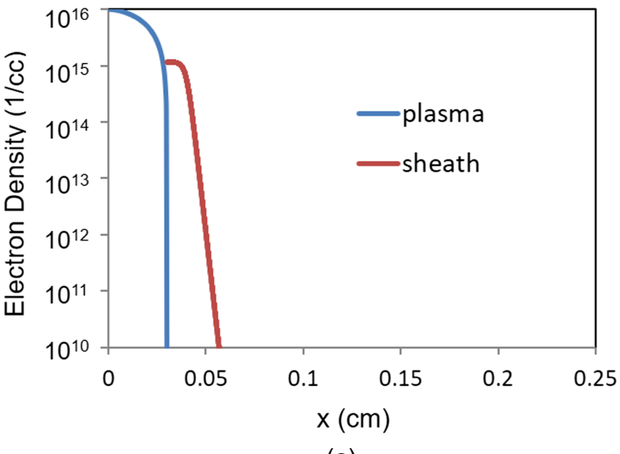

(a)

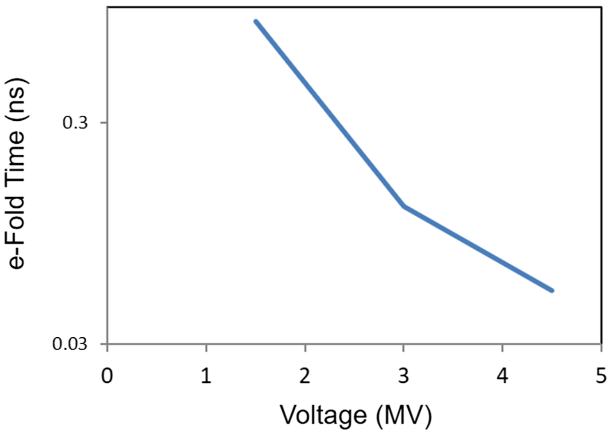

(b)

FIG. 14. Using the plasma-sheath stability model of Ref. [36], the (a) assumed resistive plasma and electron sheath density profiles are plotted and (b) the instability *e*-folding growth time is plotted assuming constant 0.7 Ohm impedance.

coaxial simulations, it produces a significantly higher σ in the direction of the plasma current, since the magnetic field is no longer purely transverse to the current. The application of a solenoidal field has a strong impact on plasma motion into the gap and subsequent current loss and should be explored for improved current delivery in next-generation *Z* pinch accelerators.

ACKNOWLEDGMENTS

The authors thank Michael Cuneo and George Laity for support of research, Edwardo Waisman for suggesting the Temkin model used in the simulations, and Robert Clark for computational physics insights. This project is partially supported by Laboratory Directed Research and Development Project No. 209240 and Contract No. 1888679 by Sandia National Laboratories. Sandia National Laboratories is a multimission laboratory managed and operated by National Technology and Engineering Solutions of Sandia, LLC, a wholly owned subsidiary of Honeywell International, Inc., for the U.S. Department of Energy's National Nuclear Security Administration under Contract No. DE-NA0003525. This paper describes objective technical results and analysis. Any subjective views or opinions that might be expressed in the paper do not necessarily represent the views of the U.S. Department of Energy or the United States Government.

[1] W. A. Stygar, M. E. Cuneo, D. I. Headley, H. C. Ives, R. J. Leeper, M. G. Mazarakis, C. L. Olson, J. L. Porter, T. C. Wagoner, and J. R. Woodworth, Phys. Rev. ST Accel. Beams **10**, 030401 (2007).

[2] D. H. McDaniel, M. G. Mazarakis, D. E. Bliss, J. M. Elizondo, H. C. Harjes, H. C. Ives, D. L. Kitterman, J. E. Maenchen, T. D. Pointon, S. E. Rosenthal, D. L. Smith, K. W. Struve, W. A. Stygar, E. A. Weinbrecht, D. L. Johnson, and J. P. Corely, in *Proceedings of the 5th International Conference on Dense Z-Pinches*, edited by J. Davis (AIP, New York, 2002), p. 23.

[3] M. E. Savage *et al.*, in *Proceedings of the 16th IEEE Pulsed Power and Plasma Science Conference, Albuquerque, NM, 2007* (IEEE, Piscataway, NJ, 2007) (Ref. [7]), p. 979.

[4] D. V. Rose, D. R. Welch, E. A. Madrid, C. L. Miller, R. E. Clark, W. A. Stygar, M. E. Savage, G. A. Rochau, J. E. Bailey, T. J. Nash, M. E. Sceiford, and K. W. Struve, Three-dimensional electromagnetic model of the pulsed-power *Z*-pinch accelerator, Phys. Rev. ST Accel. Beams **13**, 010402 (2010).

[5] D. V. Rose, E. A. Madrid, D. R. Welch, R. E. Clark, C. B. Mostrom, W. A. Stygar, and M. E. Cuneo, Computational analysis of current-loss mechanisms in a post-hole convolute driven by magnetically insulated transmission lines, Phys. Rev. ST Accel. Beams **18**, 030402 (2015).

[6] E. A. Madrid, D. V. Rose, D. R. Welch, R. E. Clark, C. B. Mostrom, W. A. Stygar, M. E. Cuneo, M. R. Gomez, T. P. Hughes, T. D. Pointon, and D. B. Seidel, Steady-state modeling of current loss in a post-hole convolute driven by high power magnetically insulated transmission lines, Phys. Rev. ST Accel. Beams **16**, 120401 (2013).

[7] D. V. Rose, D. R. Welch, C. L. Miller, R. E. Clark, E. A. Madrid, C. B. Mostrom, T. C. Wagoner, J. K. Moore, W. A. Stygar, J. E. Bailey, T. J. Nash, G. A. Rochau, and D. B. Sinars, 10^7-A load-current *B*-dot monitor: Simulations, design, and performance, Phys. Rev. ST Accel. Beams **13**, 040401 (2010).

[8] V. V. Ivanov, P. J. Laca, B. S. Bauer, R. Presura, V. I. Sotnikov, A. L. Astanovitskiy, B. LeGalloudec, J. Glassman, and R. A. Wirtz, Investigation of plasma evolution in a coaxial small-gap magnetically insulated transmission line, IEEE Trans. Plasma Sci. **32**, 1843 (2004).

[9] R. W. Stinnett, M. A. Parker, R. B. Spielman, and R. Bengtson, Small Gap Experiments in Magnetically Insulated Transmission Lines, IEEE Trans. Plasma Sci. **11**, 216 (1983).

[10] C. Thoma, D. R. Welch, R. E. Clark, D. V. Rose, and I. E. Golovkin, Hybrid-PIC modeling of laser-plasma

interactions and hot electron generation in gold hohlraum walls, Phys. Plasmas **24**, 062707 (2017).

[11] H. E. Knoepfel, *Pulse High Magnetic Fields* (Wiley, New York, 1997), ISBN 9780471885320.

[12] C. Thoma, T. C. Genoni, D. R. Welch, D. V. Rose, R. E. Clark, C. L. Miller, W. A. Stygar, and M. L. Kiefer, Numerical simulation of cathode plasma dynamics in magnetically insulated vacuum transmission lines, Phys. Plasmas **22**, 032101 (2015).

[13] J. Swegle and E. Ott, Instability of the Brillouin-Flow Equilibrium in Magnetically Insulated Structures, Phys. Rev. Lett. **46**, 929 (1981); Linear waves and instabilities on magnetically insulated gaps, Phys. Fluids **24**, 1821 (1981).

[14] D. V. Rose, T. C. Genoni, R. E. Clark, D. R. Welch, and W. A. Stygar, Electron flow stability in magnetically insulated vacuum transmission lines, Phys. Plasmas **18**, 033108 (2011).

[15] C. L. Chang, T. M. Antonsen Jr., E. Ott, and A. T. Drobot, Instabilities in magnetically insulated gaps with resistive electrode plasmas, Phys. Fluids **27**, 2545 (1984).

[16] A. B. Mikhailovskii and A. V. Timofeev, Sov. Phys. JETP **17**, 626 (1963).

[17] M. Li and H. F. Dylla, Model for the outgassing of water from metal surfaces, J. Vac. Sci. Technol. A **11**, 1702 (1993).

[18] H. F. Dylla, D. M. Manos, and P. H. LaMarche, Correlation of outgassing of stainless steel and aluminum with various surface treatments, J. Vac. Sci. Technol. A **11**, 2623 (1993).

[19] A Comptant La Fontaine, Ion emission at the target of the radiographic devices PIVAIR and AIRIX, J. Phys. D **40**, 1712 (2007).

[20] E. Waisman (private communication).

[21] A. Roth, *Vacuum Technology* (Elsevier, New York, 1990), p. 181.

[22] P. A. Redhead, Modeling the pump-down of a reversibly adsorbed phase. I. Monolayer and submonolayer initial coverage, J. Vac. Sci. Technol. A **13**, 467 (1995).

[23] D. V. Rose *et al.* (to be published).

[24] D. R. Welch, D. V. Rose, N. Bruner, R. E. Clark, B. V. Oliver, K. D. Hahn, and M. D. Johnston, Hybrid simulation of electrode plasmas in high-power diodes, Phys. Plasmas **16**, 123102 (2009).

[25] J. M. D. Lane, K. Leung, A. Thompson, and M. E. Cuneo, Water desorption from rapidly-heated metal oxide surfaces—first principles, molecular dynamics, and the Temkin isotherm, J. Phys. Condens. Matter **30**, 465002 (2018).

[26] B. I. Cohen, A. B. Langdon, and A. Friedman, Implicit time integration for plasma simulation, J. Comput. Phys. **46**, 15 (1982).

[27] D. R. Welch, D. V. Rose, B. V. Oliver, and R. E. Clark, Simulation techniques for heavy ion fusion chamber transport, Nucl. Instrum. Methods Phys. Res., Sect. A **464**, 134 (2001).

[28] T. C. Genoni, R. E. Clark, and D. R. Welch, Open Plasma Phys. J. **3**, 36 (2010).

[29] J. P. Boris, Relativistic Plasma Simulation—Optimization of a Hybrid Code, in *Proceedings of the Fourth Conference on Numerical Simulation of Plasmas, Washington DC, Naval Research Laboratory*, 1971, pp. 3–67, https://www.worldcat.org/title/proceedings-of-the-4th-conference-on-numerical-simulation-of-plasmas/oclc/27230385?referer=di&ht=edition.

[30] D. R. Welch, D. V. Rose, M. E. Cuneo, R. B. Campbell, and T. A. Mehlhorn, Integrated simulation of the generation and transport of proton beams from laser-target interaction, Phys. Plasmas **13**, 063105 (2006).

[31] B. I. Cohen, A. B. Langdon, and A. Friedman, Implicit time integration for plasma simulation, J. Comput. Phys. **46**, 15 (1982).

[32] T. W. L. Sanford, J. A. Halbleib, J. W. Poukey, A. L. Pregenzer, R. C. Pate, C. E. Heath, R. C. Mock, G. A. Mastin, D. C. Ghiglia, T. J. Roemer, P. W. Spence, and G. A. Prolux, Measurement of electron energy deposition necessary to form an anode plasma in Ta, Ti, and C for coaxial bremsstrahlung diodes, J. Appl. Phys. **66**, 10 (1989).

[33] S. A. Slutz, M. C. Herrmann, R. A. Vesey, A. B. Sefkow, D. B. Sinars, D. C. Rovang, K. J. Person, and M. E. Cuneo, Pulsed-power-driven cylindrical liner implosions of laser preheated fuel magnetized with an axial field, Phys. Plasmas **17**, 056303 (2010).

[34] C. E. Seyler, M. R. Martin, and N. D. Hamlin, Helical instability in MagLIF due to axial flux compression by low-density plasma, Phys. Plasmas **25**, 062711 (2018).

[35] T. J. Awe *et al.*, Observations of Modified Three-Dimensional Instability Structure for Imploding z-Pinch Liners that are Premagnetized with an Axial Field, Phys. Rev. Lett. **111**, 235005 (2013).

[36] D. V. Rose, T. C. Genoni, R. E. Clark, D. R. Welch, and W. E. Stygar, Electron flow stability in magnetically insulated vacuum transmission lines, Phys. Plasmas **18**, 033108 (2011).